Determining the anthropogenic greenhouse gas contribution to the observed intensification of extreme precipitation

Seungmok Paik, Seung-Ki Min, Xuebin Zhang, Markus G. Donat, Andrew D. King, & Qiaohong Sun

2020

Pacific Climate Impacts Consortium (PCIC)

PCIC Publications

© 2020 American Geophysical Union. All Rights Reserved. Distributed under AGU's publications policy: https://www.agu.org/publications/authors/policies.

Original citation:

Paik, S., Min, S., Zhang, X., Donat, M. G., King, A. D., & Sun, Q. (2020). Determining the anthropogenic greenhouse gas contribution to the observed intensification of extreme precipitation. *Geophysical Research Letters*, *47*(12), e2019GL086875. https://doi.org/10.1029/2019GL086875

Downloaded from UVicSpace Research & Learning Repository

dspace.library.uvic.ca

University of Victoria | Libraries

Check for updates

AGU ADVANCING EARTH AND SPACE SCIENCE

Geophysical Research Letters

RESEARCH LETTER
10.1029/2019GL086875

Key Points:
- Causes of the observed intensification of extreme precipitation during 1951 to 2015 are examined using CMIP6 multimodel simulations
- Results from optimal fingerprinting analyses show that the anthropogenic signals are robustly detected at hemispheric and continental scales
- The observed increase in extreme precipitation is mostly attributed to anthropogenic greenhouse gas increases

Supporting Information:
- Supporting Information S1

Correspondence to:
S.-K. Min,
skmin@postech.ac.kr

Citation:
Paik, S., Min, S.-K., Zhang, X., Donat, M. G., King, A. D., & Sun, Q. (2020). Determining the anthropogenic greenhouse gas contribution to the observed intensification of extreme precipitation. *Geophysical Research Letters*, *46*, e2019GL086875. https://doi.org/10.1029/2019GL086875

Received 1 JAN 2020
Accepted 27 APR 2020
Accepted article online 19 MAY 2020

©2020. American Geophysical Union. All Rights Reserved.

Determining the Anthropogenic Greenhouse Gas Contribution to the Observed Intensification of Extreme Precipitation

Seungmok Paik[1], Seung-Ki Min[1,2], Xuebin Zhang[3], Markus G. Donat[4], Andrew D. King[5], and Qiaohong Sun[6]

[1]Division of Environmental Science and Engineering, Pohang University of Science and Technology, Pohang, South Korea, [2]Institute for Convergence Research and Education in Advanced Technology, Yonsei University, Incheon, South Korea, [3]Climate Research Division, Environment and Climate Change Canada, Toronto, Ontario, Canada, [4]Barcelona Supercomputing Center, Barcelona, Spain, [5]School of Earth Sciences and ARC Centre of Excellence for Climate Extremes, University of Melbourne, Melbourne, Victoria, Australia, [6]Pacific Climate Impacts Consortium, University of Victoria, Victoria, British Columbia, Canada

Abstract This study conducts a detection and attribution analysis of the observed changes in extreme precipitation during 1951–2015. Observed and CMIP6 multimodel simulated changes in annual maximum daily and consecutive 5-day precipitation are compared using an optimal fingerprinting technique for different spatial scales from global land, Northern Hemisphere extratropics, tropics, three continental regions (North America and western and eastern Eurasia), and global "dry" and "wet" land areas (as defined by their average extreme precipitation intensities). Results indicate that anthropogenic greenhouse gas influence is robustly detected in the observed intensification of extreme precipitation over the global land and most of the subregions considered, all with clear separation from natural and anthropogenic aerosol forcings. Also, the human-induced greenhouse gas increases are found to be a dominant contributor to the observed increase in extreme precipitation intensity, which largely follows the increased moisture availability under global warming.

Plain Language Summary Human influences have been identified in the observed intensification of extreme precipitation at global and continental scales, but quantifying the contribution of greenhouse gas increases remains challenging. Here, we isolate anthropogenic greenhouse gas impacts on the observed intensification of extreme precipitation during 1951–2015 by comparing observations with CMIP6 individual forcing experiments. Results show that greenhouse gas influences are detected over the global land, Northern Hemisphere extratropics, western and eastern Eurasia, and global "dry" and "wet" regions, which are separable from other external forcings such as solar and volcanic activities and anthropogenic aerosols. The human-induced greenhouse gas increases are also found to explain most of the observed changes in extreme precipitation intensity, which are consistent with the increased moisture availability with warming. Our results provide the first quantitative evidence for the dominant influence of human-made greenhouse gases on extreme precipitation increase.

1. Introduction

Human-induced greenhouse gas increases have been consistently identified as the primary cause of global and regional warming in recent decades (Bindoff et al., 2013; Hegerl et al., 2007; Stott et al., 2010). Global warming is expected to increase atmospheric water holding capacity according to the Clausius-Clapeyron (C-C) relationship (~7% K^{-1}, Trenberth et al., 2003). While global mean total precipitation shows a lower increasing rate (Trenberth, 2011), due to being energetically constrained (Allen & Ingram, 2002), extreme precipitation is analyzed to increase at roughly the same rate as the moisture availability (Allen & Ingram, 2002; Kharin et al., 2013; Westra et al., 2013).

There have been many observational and model-based analyses of extreme precipitation changes under warming. Observational studies have found that extreme precipitation has intensified over many land areas in recent decades (Alexander et al., 2006; Donat et al., 2013; Groisman et al., 2005; Westra et al., 2013). Also,

19448007, 2020, 12, Downloaded from https://agupubs.onlinelibrary.wiley.com/doi/10.1029/2019GL086875 by University Of Victoria, Wiley Online Library on [10/04/2025]. See the Terms and Conditions (https://onlinelibrary.wiley.com/terms-and-conditions) on Wiley Online Library for rules of use; OA articles are governed by the applicable Creative Commons License

the frequency of heavy precipitation events has increased with warming, based on both observations and model simulations (Diffenbaugh et al., 2017; Lau et al., 2013; Lee et al., 2018). Climate models consistently project further intensification of extreme precipitation in the future in most regions with continued greenhouse gas warming (Donat et al., 2016; Kharin et al., 2013; Lau et al., 2013; Pfahl et al., 2017; Sillmann et al., 2013), which would bring a shift toward a hydroclimatic regime of more intense but less frequent daily precipitation events (Giorgi et al., 2011, 2014).

Formal detection and attribution studies have quantified the overall human contribution to the observed increase in extreme precipitation by comparing the observed and simulated changes. Min et al. (2011) detected a human influence on the observed intensification of extreme precipitation over the Northern Hemisphere (NH) land during 1951 to 1999 using the Hadley Centre global land-based climate extreme data sets (HadEX; Alexander et al., 2006) and coupled climate models from Coupled Model Intercomparison Project Phase 3 (CMIP3; Meehl et al., 2007). Zhang et al. (2013) carried out an updated detection analysis using HadEX2 (Donat et al., 2013) combined with Russian station data and CMIP5 coupled climate models (Taylor et al., 2012) over 1951 to 2005. They divided the NH into three continents and detected anthropogenic influence on the extreme precipitation increase mainly for the midlatitudes, western NH, and western Eurasia.

However, greenhouse gas influences have not previously been quantified in separation from other anthropogenic forcings like aerosols, although anthropogenic aerosols were found to have counteracting influences on mean and extreme precipitation over some regions (Lau et al., 2017; Polson et al., 2014; Wu et al., 2013). A formal analysis separating anthropogenic greenhouse gas and aerosol influences on extreme precipitation will extend our overall understanding of human influence on the climate and how that may change as these forcings evolve.

It has been suggested that global warming may change the spatial distribution of precipitation by amplifying the differences between dry and wet regions, the so-called a "dry-get-drier and wet-get-wetter (DDWW)" pattern (Held & Soden, 2006). This DDWW pattern is found over ocean, but its validity over land has been questioned (Byrne & O'Gorman, 2015; Greve et al., 2014). Recently, Donat et al. (2016) found that extreme precipitation has significantly increased over both the global dry and wet land areas over the past six decades, with dry and wet regions defined in a relative way based on the climatological precipitation amounts or extreme precipitation intensities. Generally consistent changes have been found when defining dry and wet regions based on their water availability using an Aridity Index, but uncertainties are large in particular in arid regions due to poor observational coverage (Donat et al., 2019). Rigorous optimal detection analyses have not been performed for global dry and wet lands to date.

Previous detection and attribution analyses have been performed on CMIP3 and CMIP5 multimodel ensembles (Min et al., 2011; Zhang et al., 2013), but the latest state-of-the-art global climate models from CMIP6 (Erying et al., 2016) have not been studied yet. In comparison to previous multimodel experiments, many of the CMIP6 models exhibit high climate sensitivity (e.g., Gettelman et al., 2019; Sellar et al., 2019; Swart et al., 2019; Voldoire et al., 2019) above the estimated range provided from previous Intergovernmental Panel on Climate Change (IPCC) reports (Zelinka et al., 2020). Given that much of the model-simulated change in extreme precipitation is driven by thermodynamic changes, one might expect that the response in extreme precipitation to greenhouse gas forcings in CMIP6 may differ from CMIP3 or CMIP5. It is vital to investigate past extreme precipitation changes in CMIP6 to improve understanding and usefulness of projected changes in precipitation extremes.

In this study, we have conducted an updated detection and attribution analysis of extreme precipitation changes using newly available observations and CMIP6 multimodel simulations for 1951 to 2015. Improved spatial and temporal coverage would help to detect external influences more robustly by reducing noise (Fischer et al., 2013; Min et al., 2008). This paper is structured as follows. Section 2 describes the observational data and model simulations used in this study, and the analysis methods including data processing and an optimal fingerprinting technique. Detection and attribution analysis results are provided in section 3, together with its interpretation in view of physical mechanisms. Conclusions and discussion are given in section 4.

19448007, 2020, 12, Downloaded from https://agupubs.onlinelibrary.wiley.com/doi/10.1029/2019GL086875 by University Of Victoria, Wiley Online Library on [10/04/2025]. See the Terms and Conditions (https://onlinelibrary.wiley.com/terms-and-conditions) on Wiley Online Library for rules of use; OA articles are governed by the applicable Creative Commons License

2. Data and Methods

2.1. Observational and Model Data

We used extreme precipitation indices from a stations-based observational data set, which includes 14,694 land-based observing stations with more than 30 years of record during 1900 to 2018 across the globe (Text S1 in the supporting information). These station observations are collected and assembled from various sources on which HadEX2 was based (Donat et al., 2013), and also from the national meteorological services of several countries including China, Russia, and Australia. Details are provided in Text S1.

We used multimodel climate simulations from the CMIP6 experiments to assess the extent of external forcing influences on the observed changes. First, we used the historical (ALL) simulations for 1951 to 2014, where climate models are forced with both anthropogenic (greenhouse gas and aerosol) and natural (solar and volcanic) external forcings. Each ALL simulation has been extended until 2015 by using corresponding SSP (Shared Socioeconomic Pathways) 2–4.5 scenario simulations, which represents a central pathway without substantial variations from the historical forcing (O'Neill et al., 2016). To explore the influence of individual external forcings, we also utilized historical individual forcing simulations including hist-GHG (GHG), hist-aer (AER), and hist-nat (NAT) experiments, where climate models are forced with only greenhouse gas, anthropogenic aerosol, and natural external forcing, respectively (Gillett et al., 2016). Simulations from seven CMIP6 models, which provide data for all experiments of GHG, AER, and NAT with a minimum of three ensemble members, are used in this study (Table S1). In total, there are 73 ALL runs and 35 GHG, AER, and NAT runs available for this study. Signals or model-simulated responses are computed as multimodel ensemble mean (MME); this is done by first computing the arithmetical average for each model ensemble and then averaging the individual model means. We also used 238 nonoverlapping slices of 65 years in length from each unforced preindustrial control simulation (CTL) from 27 CMIP6 models to estimate natural climate variability (Table S1).

2.2. Precipitation Indices

We used two extreme precipitation indices, the annual maxima of 1-day (Rx1day) and consecutive 5-day (Rx5day) precipitation, from the observations and CMIP6 simulations. The magnitude of the extreme precipitation indices varies across regions, which could make spatial averages dominated by wetter regions. To avoid such overrepresentation of wet regions in spatial aggregations, we converted observed and simulated Rx1day and Rx5day values to a "probability-based index" (PI). The PI was calculated by fitting a generalized extreme value (GEV) distribution on Rx1day or Rx5day data at each grid cell and obtaining the corresponding values of the fitted cumulative density function following previous studies (Min et al., 2009, 2011; Zhang et al., 2013). Resulting PI values range from 0 to 1 where high values (closer to 1) represent more extreme precipitation and low values (closer to 0) represent weaker extreme precipitation. To consider long-term changes, we first selected 5,922 stations, which have records longer than 70% during 1951–2015 and at least 3 years of record during 2011–2015. Rx1day and Rx5day from the selected station data sets are converted to PI and then interpolated onto 5.0° × 5.0° grid boxes using simple averages (when at least one station exists within each grid box). Figure 1 shows the spatial distribution of the available observational data (note that Rx1day and Rx5day have the same data coverage).

Model-simulated Rx1day and Rx5day values were similarly converted to PI on each original grid and then interpolated onto the same observational grids. The interpolated model data sets were then masked according to the availability of observational data. For detection analysis, we calculated nonoverlapping 5-year means of the PI averaged over global land (GLB), NH extratropics (NHE, north of 30°N), tropics (TR, 30°S to 30°N), and three continental regions from NH including western NH (NA, 45–180°W), western Eurasia (EU, 25°W to 60°E), and eastern Eurasia (AS, 60–180°E) (Figure 1). Note that GLB is dominated by NHE in this station-based data set. We defined global "dry" and "wet" regions as the regions where values are smaller or greater than median grid values of all land grid cells based on the observed climatology for 1961–2000 for each extreme precipitation index, similar to Donat et al. (2016). Note that Rx1day and Rx5day have very similar "dry" and "wet" regions but there are some differences (Figure 1), due to the different spatial patterns of their climatologies.

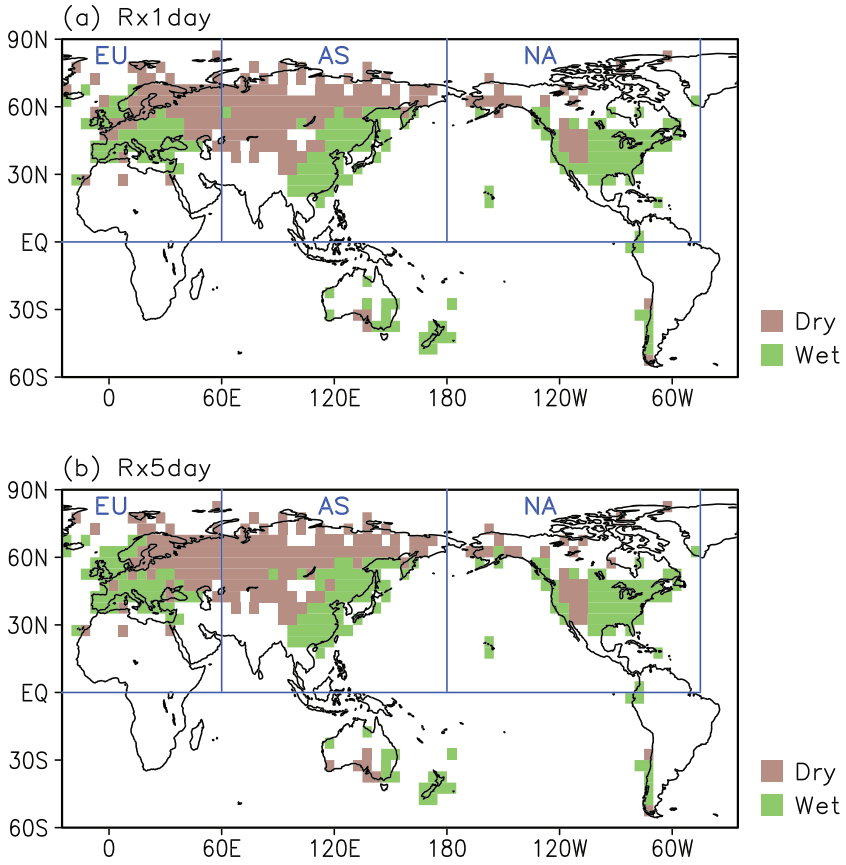

Figure 1. Spatial distribution of observational data coverage for (a) Rx1day and (b) Rx5day. Location of grids with observations having more than 70% records during 1951 to 2015 plus minimum 3 years during 2011 to 2015. The blue lines delineate three continental domains and brown and green colored grids indicate global 'dry' and 'wet' regions, respectively. See text for details.

2.3. Optimal Fingerprinting Detection Analysis

We employed an optimal fingerprinting technique as a method for detection and attribution analysis to compare observed PI changes to model simulations, in which observations ($\boldsymbol{y}$) are regressed onto model simulated signals $\mathbf{X}$ via a total least squares method (Allen & Stott, 2003) such that $\boldsymbol{y} = (\mathbf{X} - \boldsymbol{\nu})\,\boldsymbol{\beta} + \boldsymbol{\varepsilon}$. Here, $\boldsymbol{\varepsilon}$ represents internally generated residual variability, and $\boldsymbol{\nu}$ is the noise component of $\mathbf{X}$. The fingerprints $\mathbf{X}$ are estimated from CMIP6 multimodel means for the different forced runs (ALL, GHG, AER, and NAT). The variance-covariance matrix of ε is obtained from CTL chunks, and $\boldsymbol{\nu}$ is assumed to be proportional to $\boldsymbol{\varepsilon}$. The 65-year CTL chunks are divided into two sets, and the first set is used to get best estimates of the scaling factor $\boldsymbol{\beta}$, and the second set is used to estimate the 5–95% uncertainty range of $\boldsymbol{\beta}$ and also to carry out a residual consistency test (Allen & Stott, 2003). Detection is declared when the 90% uncertainty range of a scaling factor is above zero, which implies a significant relationship between observed change and fingerprint patterns. We employed a residual consistency test to consider model skill for internal variability amplitude. If the modeled internal variability (estimated from CTL) is too small, the uncertainty range of the scaling factors would be underestimated, leading to spurious detection. To avoid this, we compared model-simulated internal variability with observational residual variance following Allen and Tett (1999).

We conducted two-signal detection analysis by regressing the observed changes onto the anthropogenic signals (ANT, which are estimated as ALL minus NAT) and NAT simultaneously. More importantly, using the CMIP6 individual forcing runs, we carried out three-signal optimal detection analysis in which observations are regressed onto GHG, AER, and NAT signals simultaneously. This two- or three-way regression analysis enables us to examine whether multiple signals are jointly detected and whether the detected signal is separable from other external factors as well as internal variability noise. Based on the multisignal analysis,

19448007, 2020, 12, Downloaded from https://agupubs.onlinelibrary.wiley.com/doi/10.1029/2019GL086875 by University Of Victoria, Wiley Online Library on [10/04/2025]. See the Terms and Conditions (https://onlinelibrary.wiley.com/terms-and-conditions) on Wiley Online Library for rules of use; OA articles are governed by the applicable Creative Commons License

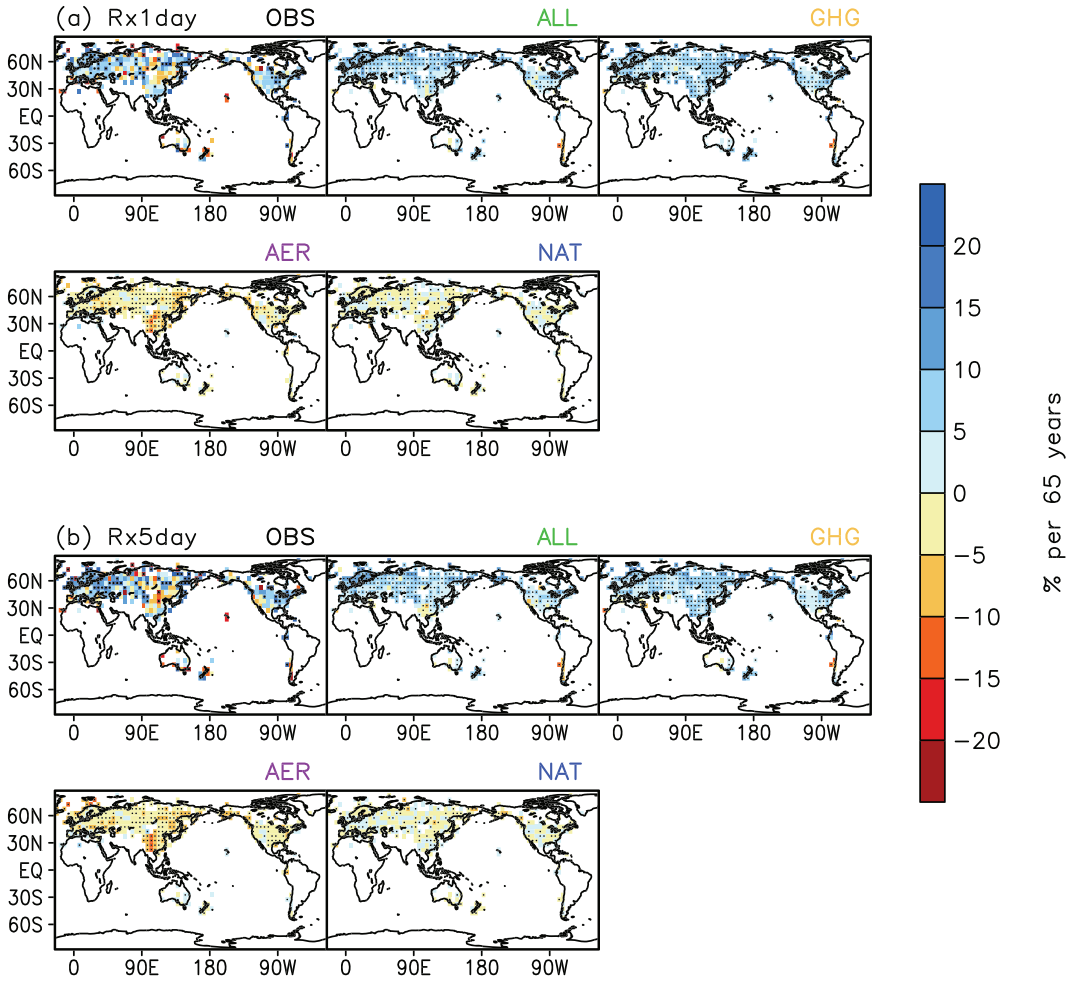

Figure 2. Spatial patterns of long-term trends in (a) Rx1day and (b) Rx5day (using a probability-based index, PI) during 1951–2015 from observations (OBS), CMIP6 multimodel simulations with anthropogenic plus natural forcing (ALL), only greenhouse gas (GHG), anthropogenic aerosol (AER), and natural forcing (NAT). Black dots indicate grids where long-term trends are significant at the 5% level based on *t* test in observations or more than five models have equal sign of the responses among seven CMIP6 models (Table S1).

attributable changes to each signal are estimated by multiplying the obtained scaling factors with long-term trends of fingerprints (Hegerl & Zwiers, 2011).

3. Results

3.1. Observed and Modeled Trends

Figure 2 illustrates spatial patterns of the observed and CMIP6 MME-simulated trends of PI for Rx1day and Rx5day over 1951 to 2015. Observations show significant increases especially over NH extratropics, while the trends are uncertain especially over Asia and Southern Hemisphere. The MMEs from ALL simulations show positive trends for a large part of the global land, and trends are greater over the NH extratropics with large intermodel consistency regarding the sign of the response. GHG also has increasing trends in most regions with stronger amplitudes than ALL. AER has a counteracting influence especially over Asia as shown by Lau et al. (2017), causing the weaker increase in extreme precipitation in ALL than in GHG. NAT simulations exhibit only small long-term trends. Results for Rx1day and Rx5day show very similar patterns for both observations and CMIP6 simulations.

Area-averaged Rx1day and Rx5day PI time series of observations and CMIP6 MME are illustrated in Figure 3 over global land (GLB), two broad zonal regions (NHE and TR), three NH continents (NA, EU, and AS), and

19448007, 2020, 12, Downloaded from https://agupubs.onlinelibrary.wiley.com/doi/10.1029/2019GL086875 by University Of Victoria, Wiley Online Library on [10/04/2025]. See the Terms and Conditions (https://onlinelibrary.wiley.com/terms-and-conditions) on Wiley Online Library for rules of use; OA articles are governed by the applicable Creative Commons License

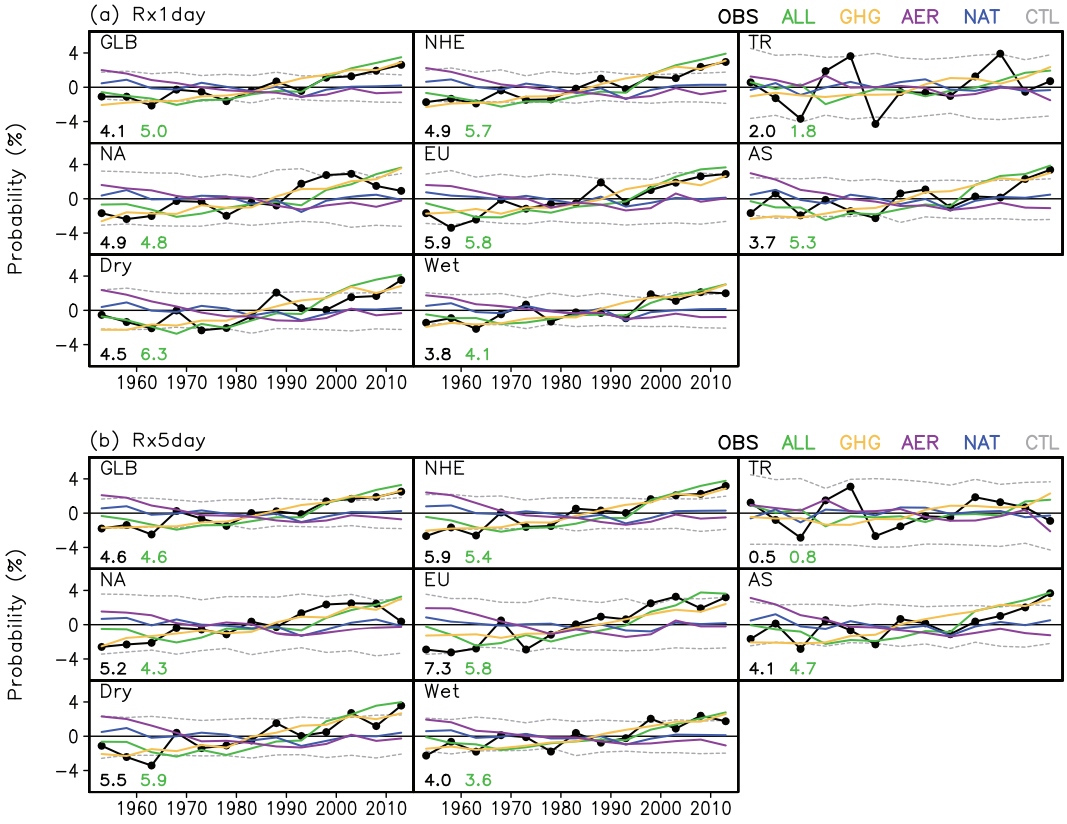

Figure 3. Time series of 5-year mean area-averaged PI of (a) Rx1day and (b) Rx5day from observations (OBS, black) and CMIP6 multimodel simulations with anthropogenic plus natural (ALL, green), only greenhouse gas (GHG, yellow), anthropogenic aerosol (AER, purple), natural forcing (NAT, blue) over global land (GLB), two broad zonal regions (NHE and TR), three continents (NA, EU, and AS), and global "dry" and "wet" regions (Dry and Wet) classified from the climatological precipitation characteristics. Gray dashed lines represent the 5% to 95% range of internal variability estimated from control (CTL) simulations. Amplitudes of long-term trends (% per 65 years) of OBS and ALL are presented together at the bottom of each plot.

global "dry" and "wet" land regions. In observations, statistically significant ($p < 0.01$) increasing trends are found over all the individual domains except for TR for both extreme indices. "Dry" regions tend to have greater intensification of extreme precipitation than "wet" regions, which might be due to stronger warming in middle-to-high latitudes (Jones et al., 2013), which occupy a large part of the global "dry" regions (Figure 1). Nonsignificant trends over TR are due to large internal variability, which seems to be partly related to smaller domains (Figure 1). ALL and GHG reproduce the observed increase in extreme precipitation for the regions with significant observed trends. Slight overestimation of the increases occurs for GLB and NHE for Rx1day as found by Zhang et al. (2013). AER time series exhibits counteracting decreasing trends in extreme precipitation intensity, especially over the AS, as can be seen from the spatial patterns of trends (Figure 2).

3.2. Detection and Attribution Analysis Results

Figure 4a shows best estimates and 5–95% uncertainty ranges of the scaling factors for GHG, AER, and NAT in three-signal analyses over individual regions. Results show that the anthropogenic greenhouse gas influence is significantly detected and separable from AER and NAT for Rx1day over AS and "wet" regions, for Rx5day over GLB, and for both indices over NHE, EU, and "dry" regions. GHG signals are not detectable over TR and NA, presumably due to larger internal variability and intermodel uncertainties over the tropics (O'Gorman & Schneider, 2009; Westra et al., 2013). However, ANT signals are detected for all domains except TR in two-signal analysis (Figure S1). For GLB and NHE, scaling factors include unity, indicating that the observed changes are largely explained by GHG forcing. However, best estimates of the scaling factors for GHG and ANT are smaller than unity, indicating that CMIP6 models overestimate the observed increase in

19448007, 2020, 12, Downloaded from https://agupubs.onlinelibrary.wiley.com/doi/10.1029/2019GL086875 by University Of Victoria, Wiley Online Library on [10/04/2025]. See the Terms and Conditions (https://onlinelibrary.wiley.com/terms-and-conditions) on Wiley Online Library for rules of use; OA articles are governed by the applicable Creative Commons License

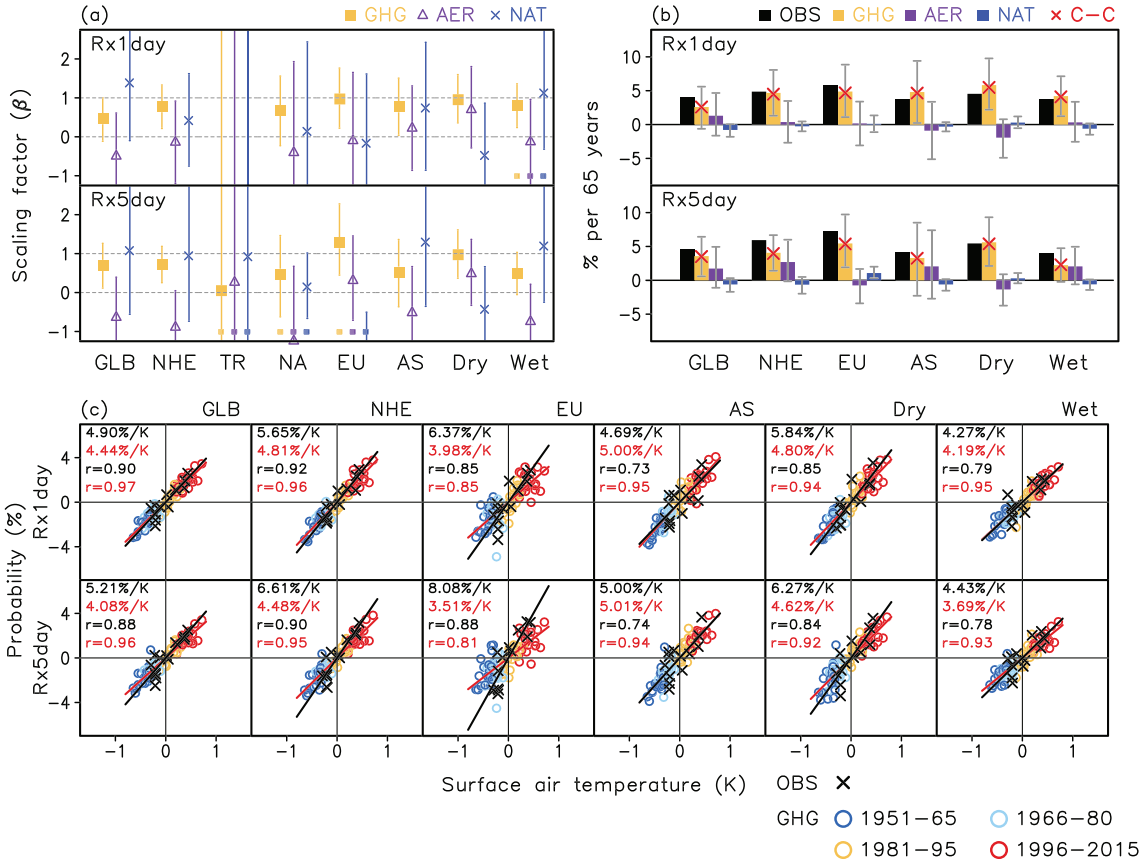

Figure 4. (a) Results from the three-signal optimal detection analyses of Rx1day (top) and Rx5day (bottom) over global land, zonal-averaged, continental scales as well as "dry" and "wet" regions over 1951 to 2015. Best estimates (data points) and 5–95% uncertainty ranges (error bars) of scaling factors (β) are displayed for GHG (yellow), AER (purple), and NAT (blue) signals. The two gray dashed horizontal lines indicate zero and unity. Squares indicate the failure of the residual consistency test due to too large model variability. (b) Observed (black) trends compared with attributable trends due to GHG, AER, and NAT forcings for spatial domains where GHG signals are detected. Red x marks represent extreme precipitation increases explained by Clausius-Clapeyron relation (see text for details). (c) Scatter plots of 5-year mean PI anomalies (y axis) of Rx1day (top) and Rx5day (bottom) and globally averaged SAT (x axis) during 1951–2015 from observation (black x mark) and CMIP6 hist-GHG simulations (colored circles). Blue, light blue, yellow, and red circles represent the 5-year mean anomalous values obtained from 1951–1965, 1966–1980, 1981–1995, and 1996–2015 periods, respectively. Regression coefficients from observations (black) and model simulations (red) are provided with correlations estimated from models values.

extreme precipitation (see below for discussion related to the higher climate sensitivity in CMIP6). This is consistent with the finding of Zhang et al. (2013) especially for Rx1day based on CMIP5 models for a shorter period. The AER and NAT signals are not detected over most of the domains. Donat et al. (2016) showed extreme precipitation increases over both "dry" and "wet" land regions, and our results confirm that those increases are due to GHG influences. Simple analysis of signal-to-noise ratios (Table S2) shows that all domains with GHG signal detection indeed have stronger signal (defined as linear trend slopes) than noise (estimated as ±1 standard deviation ranges of linear trends from CTL chunks).

Using the estimated scaling factors, we obtained attributable trends in extreme precipitation over 1951 to 2015 for the domains where GHG signals are detected (Figure 4b). On the basis of the MME responses, results show that the observed increases in extreme precipitation over the global land, NH extratropics, western and eastern Eurasia, and global "dry" and "wet" regions are largely explained by GHG influence. AER and NAT signals exert much weaker influences with different signs across regions. Considering that extreme precipitation generally intensifies with warming following the C-C relation, we have examined the relationship between extreme precipitation changes and global mean surface air temperature (SAT) changes (Figure 4c). The 5-year mean PI values are regressed onto the global mean SAT for observations and GHG simulations. Modeled SAT is interpolated onto 5° × 5° resolution and then masked with observational

19448007, 2020, 12, Downloaded from https://agupubs.onlinelibrary.wiley.com/doi/10.1029/2019GL086875 by University Of Victoria, Wiley Online Library on [10/04/2025]. See the Terms and Conditions (https://onlinelibrary.wiley.com/terms-and-conditions) on Wiley Online Library for rules of use; OA articles are governed by the applicable Creative Commons License

19448007, 2020, 12, Downloaded from https://agupubs.onlinelibrary.wiley.com/doi/10.1029/2019GL086875 by University Of Victoria, Wiley Online Library on [10/04/2025]. See the Terms and Conditions (https://onlinelibrary.wiley.com/terms-and-conditions) on Wiley Online Library for rules of use; OA articles are governed by the applicable Creative Commons License

coverage (HadCRUT4; Morice et al., 2012) before analysis. Observations show regression slopes of 4.90% and 5.21% K^{-1} for Rx1day and Rx5day over the global land. The NH extratropics have slightly greater slopes (5.65% and 6.61% K^{-1}). GHG simulations capture the observed relation but with slight underestimation (4% to 5% K^{-1} for GLB and NHE). Over the western and eastern Eurasia and "dry" and "wet" regions, observations and GHG runs exhibit wider ranges of regression coefficients ranging from around 3.5% to 8.1% K^{-1}.

It should be noted that the regression slopes obtained here cannot be directly compared with the expected slope from the C-C relation, since it is based on PI rather than percent change of extreme precipitation amount. However, we find that PI variations are quite similar to percent change of extreme precipitation for both observations and CMIP6 models, showing overall one-to-one relation (Figures S2a and S2b). When calculating the slope using percent change of extreme precipitation (Figures S2c and S2d), they become similar to 7% K^{-1} over GLB and NHE in observations while CMIP6 models exhibit lower values. We further estimate the warming-driven (thermodynamic) portion of extreme precipitation increases by multiplying the estimated slope with SAT changes during 1951–2015 and scaling it with best estimates of β in Figure 4a. The results (Figure 4b) show that the GHG-induced intensification of extreme precipitation is consistent with the warming-driven increase, supporting the dominance of thermodynamic contributions at these spatial scales (Min et al., 2011; Zhang et al., 2013).

3.3. Sensitivity Test

To assess the robustness of our detection results, we have conducted several sensitivity tests to the possible uncertainty factors related to observations and model sampling. First, similar results were obtained when using HadEX3 (https://www.metoffice.gov.uk/hadobs/hadex3) as observations for 1951–2010 (analysis domain shown in Figure S3), with GHG signals additionally detected over TR for Rx5day but no detection over "wet" regions (Figure S4). Second, when considering spatial patterns in global analysis by combining two regions (NHE + TR or "dry" + "wet", 26 dimensions) or three regions (NA + EU + AS, 39 dimensions), detection results remain similar (Figure S5). Finally, our results are found to be insensitive to the model sampling. In particular, we compared models with different climate sensitivity based on the equilibrium climate sensitivity (ECS, a hypothetical value of global warming at equilibrium for a doubling of carbon dioxide) from CMIP6 models. Many CMIP6 models exhibit large ECS above the estimated range from CMIP5 (Zelinka et al., 2020). Particularly, three of seven common models (CanESM5, CNRM-CM6-1, and HadGEM3-GC31-LL) are found to have ECS above the CMIP5 models range. However, global land mean SAT and extreme precipitation trends do not show a clear monotonic association with the order of ECS (Figure S6), and three-signal detection results are not different between the two model groups with stronger and weaker ECS (Figure S7). However, we note this test is based on only seven models and a more robust analysis will only be possible when more model simulations become available.

Using higher-resolution climate simulations may result in improved simulation of precipitation and related mesoscale systems and atmospheric circulation relative to coarse-grain models (e.g., DeAngelis et al., 2013; Roberts et al., 2018; van Haren, Haarsma, de Vries, et al., 2015; van Haren, Haarsma, van Oldenborgh, et al., 2015). To examine possible influences of model resolution on extreme precipitation, we have conducted a preliminary analysis using available historical (ALL) simulations from High Resolution Model Intercomparison Project (HighResMIP; Haarsma et al., 2016). Using three models with a minimum of three ensemble members (Figure S8), long-term means and trends in Rx1day averaged over GLB are compared across simulations under different horizontal resolution for each model. Results indicate that higher-resolution runs tend to simulate on average higher extreme precipitation intensities (Figure S8a), consistent with previous studies cited above. However, there seems no systematic influence of horizontal resolution on the trend amplitudes, indicating that higher resolution does not necessarily intensify the larger-scale long-term trends in extreme precipitation (Figures S8b and S8c). Further, the extreme precipitation trend (% based on PI) relative to global warming (Figure S8d) is found to remain similar between different resolutions although different models show different change rates (4–7% K^{-1}). This basic examination using available high-resolution model simulations supports the dominant role of thermodynamic effects such that large-scale long-term trends in extreme precipitation primarily follow increases in atmospheric moisture availability with global warming (Allen & Ingram, 2002; Kharin et al., 2013; Westra et al., 2013). Further analysis based on a larger set of high-resolution simulations would allow for more robust analysis than is possible currently.

19448007, 2020, 12, Downloaded from https://agupubs.onlinelibrary.wiley.com/doi/10.1029/2019GL086875 by University Of Victoria, Wiley Online Library on [10/04/2025]. See the Terms and Conditions (https://onlinelibrary.wiley.com/terms-and-conditions) on Wiley Online Library for rules of use; OA articles are governed by the applicable Creative Commons License

4. Summary and Conclusions

This study performs a formal detection and attribution analysis of the observed intensification of extreme precipitation by comparing observations and CMIP6 multimodel simulations for 1951–2015 using an optimal fingerprinting technique. In particular, this is the first study to isolate the greenhouse gas contribution to the observed changes with clear separation from other forcing factors. Using three-signal analysis that considers greenhouse gas, anthropogenic aerosols, and natural (solar and volcanic) forcings simultaneously, we show that the greenhouse gas signal in the observed changes is detected over the global land, NH extratropics, western and eastern Eurasia, and global "dry" and "wet" land regions.

When quantifying attributable trends of the observed changes to external forcings based on three-signal analysis results, most of the observed increasing trends in extreme precipitation are found to be explained by anthropogenic greenhouse gas forcing with anthropogenic aerosols and natural forcings having marginal influences. Further, the greenhouse gas-induced changes are consistent with the expected physical mechanism of extreme precipitation intensification following atmospheric moisture increase under warming via the C-C relation.

Sensitivity tests to the use of different observations and model sampling show overall similar results, suggesting that we can have a degree of confidence in the main conclusions of our analysis. Further confirmation of our findings and analysis of the effects of higher model climate sensitivity is needed, but this will only be possible when more model runs are available. Also, a caveat remains related to the use of relatively coarse-resolution models that do not resolve relevant mesoscale processes associated with heavy precipitation events. A basic examination using a few higher-resolution models shows no sensitivity of long-term changes to the available model resolutions and supports the important role of thermodynamic effect in determining large-scale extreme precipitation trends, but a more comprehensive investigation is warranted based on individual forcing simulations with more models.

The increases in extreme precipitation have important implications since they might lead to increased risk of floods and effects on ecosystems and agriculture as warming continues (Field et al., 2014). Especially, for dry regions where high-intensity extreme precipitation events do not occur often, the intensification of extreme precipitation can have greater impacts in the future unless proper adaptation is implemented.

Acknowledgments

This study is supported by the Korea Meteorological Administration Research and Development Program under Grant KMI2018-03610 and by a National Research Foundation of Korea (NRF) grant funded by the South Korean government (MSIT) (NRF-2018R1A5A1024958). M. G. D. is grateful for funding by the Spanish Ministry for the Economy, Industry and Competitiveness Ramón y Cajal 2017 grant (reference RYC-2017-22964) and the Horizon 2020 EUCP project (Grant Agreement 776613). A. D. K. receives funding from the Australian Research Council (DE180100638). We acknowledge the World Climate Research Programme, which, through its Working Group on Coupled Modelling, coordinated and promoted CMIP6. We thank the climate modeling groups for producing and making available their model output, the Earth System Grid Federation (ESGF) for archiving the data and providing access (https://esgf-node.llnl.gov/projects/cmip6/), and the multiple funding agencies who support CMIP6 and ESGF.

References

Alexander, L. V., Zhang, X., Peterson, T. C., Caesar, J., Gleason, B., Klein Tank, A. M. G., et al. (2006). Global observed changes in daily climate extremes of temperature and precipitation. *Journal of Geophysical Research*, *111*, D05109. https://doi.org/10.1029/2005JD006290

Allen, M. R., & Ingram, W. J. (2002). Constraints on future changes in climate and the hydrological cycle. *Nature*, *419*(6903), 228–232. https://doi.org/10.1038/nature01092

Allen, M. R., & Stott, P. A. (2003). Estimating signal amplitudes in optimal fingerprinting, Part I: Theory. *Climate Dynamics*, *21*(5–6), 477–491. https://doi.org/10.1007/s00382-003-0313-9

Allen, M. R., & Tett, S. F. B. (1999). Checking for model consistency in optimal fingerprinting. *Climate Dynamics*, *15*(6), 419–434. https://doi.org/10.1007/s003820050291

Bindoff, N. L., Stott, P. A., AchutaRao, K. M., Allen, M. R., Gillett, N., Gutzler, D., et al. (2013). Detection and attribution of climate change: From global to regional. In T. F. Stocker, et al. (Eds.), *Climate Change 2013: The Physical Science Basis. Contribution of Working Group I to the Fifth Assessment Report of the Intergovernmental Panel on Climate Change* (pp. 867–952). Cambridge, UK and New York: Cambridge University Press.

Byrne, M. P., & O'Gorman, P. A. (2015). The response of precipitation minus evapotranspiration to climate warming: Why the "wet-get-wetter, dry-get-drier" scaling does not hold over land. *Journal of Climate*, *28*(20), 8078–8092. https://doi.org/10.1175/JCLI-D-15-0369.1

DeAngelis, A. M., Broccoli, A. J., & Decker, S. G. (2013). A comparison of CMIP3 simulations of precipitation over North America with observations: Daily statistics and circulation features accompanying extreme events. *Journal of Climate*, *26*(10), 3209–3230. https://doi.org/10.1175/JCLI-D-12-00374.1

Diffenbaugh, N. S., Singh, D., Mankin, J. S., Horton, D. E., Swain, D. L., Touma, D., et al. (2017). Quantifying the influence of global warming on unprecedencted extreme climate events. *Proceedings of the National Academy of Sciences of the United States of America*, *114*(19), 4881–4886. https://doi.org/10.1073/pnas.1618082114

Donat, M. G., Alexander, L. V., Yang, H., Durre, I., Vose, R., Dunn, R. J. H., et al. (2013). Updated analyses of temperature and precipitation extreme indices since the beginning of the twentieth century: The HadEX2 dataset. *Journal of Geophysical Research: Atmospheres*, *118*, 2098–2118. https://doi.org/10.1002/jgrd.50150

Donat, M. G., Angélil, O., & Ukkola, A. M. (2019). Intensification of precipitation extremes in the world's humid and water-limited regions. *Environmental Research Letters*, *14*, 065003. https://doi.org/10.1088/1748-9326/ab1c8e

Donat, M. G., Lowry, A. L., Alexander, L. V., O'Gorman, P. A., & Maher, N. (2016). More extreme precipitation in the world's dry and wet regions. *Nature Climate Change*, *6*(5), 508–513. https://doi.org/10.1038/nclimate2941

Erying, V., Bony, S., Meehl, G. A., Senior, C. A., Stevens, B., Stouffer, R. J., & Taylor, K. E. (2016). Overview of the Coupled Model Intercomparison Poroject Phase 6 (CMIP6) experimental design and organization. *Geoscientific Model Development*, *9*(5), 1937–1958. https://doi.org/10.5194/gmd-9-1937-2016

Field, C. B., Barros, V. R., Dokken, D. J., Mach, K. J., Mastrandrea, M. D., Bilir, T. E., et al. (Eds) (2014). *Climate Change 2014: Impacts, adaptation, and vulnerability. Part A: Global and sectoral aspects. Contribution of Working Group II to the Fifth Assessment Report of the Intergovernmental Panel on Climate Change.* Cambridge, UK and New York: Cambridge University Press.

Fischer, E. M., Beyerle, U., & Knutti, R. (2013). Robust spatially aggregated projections of climate extremes. *Nature Climate Change*, *3*(12), 1033–1038. https://doi.org/10.1038/nclimate2051

Gettelman, A., Hannay, C., Bacmeister, J. T., Neale, R. B., Pendergrass, A. G., Danabasoglu, G., et al. (2019). High climate sensitivity in the Community Earth System Model Version 2 (CESM2). *Geophysical Research Letters*, *46*, 8329–8337. https://doi.org/10.1029/2019GL083978

Gillett, N. P., Shiogama, H., Funke, B., Hegerl, G., Knutti, R., Matthes, K., et al. (2016). The Detection and Attribution Model Intercomparison Project (DAMIP v1.0) contribution to CMIP6. *Geoscientific Model Development*, *9*(10), 3685–3697. https://doi.org/10.5194/gmd-9-3685-2016

Giorgi, F., Coppola, E., & Raffaele, F. (2014). A consistent picture of the hydroclimatic responses to global warming from multiple indices: Models and observations. *Journal of Geophysical Research: Atmospheres*, *119*, 11,695–11,708. https://doi.org/10.1002/2014JD022238

Giorgi, F., Im, E.-S., Coppola, E., Diffenbaugh, N. S., Gao, X. J., Mariotti, L., & Shi, Y. (2011). Higher hydroclimatic intensity with global warming. *Journal of Climate*, *24*(20), 5309–5324. https://doi.org/10.1175/2011JCLI3979.1

Greve, P., Orlowsky, B., Mueller, B., Sheffield, J., Reichstein, M., & Seneviratne, S. I. (2014). Global assessment of trends in wetting and drying over land. *Nature Geoscience*, *7*(10), 716–721. https://doi.org/10.1038/ngeo2247

Groisman, P. Y., Knight, R. W., Easterling, D. R., Karl, T. R., Hegerl, G. C., & Razuvaev, V. N. (2005). Trends in intense precipitation in the climate record. *Journal of Climate*, *18*(9), 1326–1350. https://doi.org/10.1175/JCLI3339.1

Haarsma, R. J., Roberts, M. J., Vidale, P. L., Senior, C. A., Bellucci, A., Bao, Q., et al. (2016). High Resolution Model Intercomparison Project (HighResMIP v1.0) for CMIP6. *Geoscientific Model Development*, *9*(11), 4185–4208. https://doi.org/10.5194/gmd-9-4185-2016

Hegerl, G., & Zwiers, F. (2011). Use of models in detection and attribution of climate change. *Wiley Interdisciplinary Reviews: Climate Change*, *2*(4), 570–591. https://doi.org/10.1002/wcc.121

Hegerl, G. C., Zwiers, F. W., Braconnot, P., Gillett, N. P., Luo, Y., Marengo Orsini, J. A., et al. (2007). Understanding and attributing climate change. In S. Solomon, D. Qin, M. Manning, Z. Chen, M. Marquis, K. B. Averyt, et al. (Eds.), *Climate change 2007: The physical science basis. Contribution of Working Group I to the Fourth Assessment Report of the Intergovernmental Panel on Climate Change* (pp. 663–745). Cambridge, UK and New York: Cambridge University Press.

Held, I. M., & Soden, B. J. (2006). Robust responses of the hydrological cycle to global warming. *Journal of Climate*, *19*(21), 5686–5699. https://doi.org/10.1175/JCLI3990.1

Jones, G. S., Stott, P. A., & Christidis, N. (2013). Attribution of observed historical near-surface temperature variations to anthropogenic and natural causes using CMIP5 simulations. *Journal of Geophysical Research: Atmospheres*, *118*, 4001–4024. https://doi.org/10.1002/jgrd.50239

Kharin, V. V., Zwiers, F. W., Zhang, X., & Wehner, M. (2013). Changes in temperature and precipitation extremes in the CMIP5 ensemble. *Climatic Change*, *119*(2), 345–357. https://doi.org/10.1007/s10584-013-0705-8

Lau, W. K. M., Kim, K.-M., & Leung, L. R. (2017). Changing circulation structure and precipitation characteristics in Asian monsoon regions: Greenhouse warming vs. aerosol effects. *Geoscience Letters*, *4*, 28. https://doi.org/10.1186/s40562-017-0094-3

Lau, W. K.-M., Wu, H.-T., & Kim, K.-M. (2013). A canonical response of precipitation characteristics to global warming from CMIP5 models. *Geophysical Research Letters*, *40*, 3163–3169. https://doi.org/10.1002/grl.50420

Lee, D., Min, S.-K., Fischer, E., Shiogama, H., Bethke, I., Lierhammer, L., & Scinocca, J. F. (2018). Impacts of half a degree additional warming on the Asian summer monsoon rainfall characteristics. *Environmental Research Letters*, *13*, 044033. https://doi.org/10.1088/1748-9326/aab55d

Meehl, G. A., Covey, C., Delworth, T., Latif, M., McAvaney, B., Mitchell, J. F. B., et al. (2007). The WCRP CMIP3 multimodel dataset: A new era in climatic change research. *Bulletin of the American Meteorological Society*, *88*(9), 1383–1394. https://doi.org/10.1175/BAMS-88-9-1383

Min, S.-K., Zhang, X., Zwiers, F. W., & Agnew, T. (2008). Human influence on Arctic sea ice detectable from early 1990s onwards. *Geophysical Research Letters*, *35*, L21701. https://doi.org/10.1029/2008GL035725

Min, S.-K., Zhang, X., Zwiers, F. W., Friederichs, P., & Hense, A. (2009). Signal detectability in extreme precipitation changes assessed from twentieth century climate simulations. *Climate Dynamics*, *32*(1), 95–111. https://doi.org/10.1007/s00382-008-0376-8

Min, S.-K., Zhang, X., Zwiers, F. W., & Hegerl, G. C. (2011). Human contribution to more-intense precipitation extremes. *Nature*, *470*(7334), 378–381. https://doi.org/10.1038/nature09763

Morice, C. P., Kennedy, J. J., Rayner, N. A., & Jones, P. D. (2012). Quantifying uncertainties in global and regional temperature change using an ensemble of observational estimates: The HadCRUT4 data set. *Journal of Geophysical Research*, *117*, D08101. https://doi.org/10.1029/2011JD017187

O'Gorman, P. A., & Schneider, T. (2009). The physical basis for increases in precipitation extremes in simulations of 21st-century climate change. *Proceedings of the National Academy of Sciences of the United States of America*, *106*(35), 14,773–14,777. https://doi.org/10.1073/pnas.0907610106

O'Neill, B. C., Tebaldi, C., van Vuuren, D. P., Eyring, V., Friedlingstein, P., Hurtt, G., et al. (2016). The Scenario Model Intercomparison Project (ScenarioMIP) for CMIP6. *Geoscientific Model Development*, *9*(9), 3461–3482. https://doi.org/10.5194/gmd-9-3461-2016

Pfahl, S., O'Gorman, P. A., & Fischer, E. M. (2017). Understanding the regional pattern of projected future changes in extreme precipitation. *Nature Climate Change*, *7*(6), 423–427. https://doi.org/10.1038/nclimate3287

Polson, D., Bollasina, M., Hegerl, G. C., & Wilcox, L. J. (2014). Decreased monsoon precipitation in the Northern Hemisphere due to anthropogenic aerosols. *Geophysical Research Letters*, *41*, 6023–6029. https://doi.org/10.1002/2014GL060811

Roberts, M. J., Vidale, P. L., Senior, C., Hewitt, H. T., Bates, C., Berthou, S., et al. (2018). The benefits of global high resolution for climate simulation: Process understanding and the enabling of stakeholder decisions at the regional scale. *Bulletin of the American Meteorological Society*, *99*(11), 2341–2359. https://doi.org/10.1175/BAMS-D-15-00320.1

Sellar, A. A., Jones, C. G., Mulcahy, J. P., Tang, Y., Yool, A., Wiltshire, A., et al. (2019). UKESM1: Description and evaluation of the U.K. Earth System Model. *Journal of Advances in Modeling Earth Systems*, *11*(12), 4513–4558. https://doi.org/10.1029/2019MS001739

Sillmann, J., Kharin, V. V., Zwiers, F. W., Zhang, X., & Bronaugh, D. (2013). Climate extremes indices in the CMIP5 multimodel ensemble: Part 2. Future climate projections. *Journal of Geophysical Research: Atmospheres*, *118*, 2473–2493. https://doi.org/10.1002/jgrd.50188

Stott, P. A., Gillett, N. P., Hegerl, G. C., Karoly, D. J., Stone, D. A., Zhang, X., & Zwiers, F. (2010). Detection and attribution of climate change: A regional perspective. *Wiley Interdisciplinary Reviews: Climate Change*, *1*(2), 192–211. https://doi.org/10.1002/wcc.34

19448007, 2020, 12, Downloaded from https://agupubs.onlinelibrary.wiley.com/doi/10.1029/2019GL086875 by University Of Victoria, Wiley Online Library on [10/04/2025]. See the Terms and Conditions (https://onlinelibrary.wiley.com/terms-and-conditions) on Wiley Online Library for rules of use; OA articles are governed by the applicable Creative Commons License

Swart, N. C., Cole, J. N. S., Kharin, V. V., Lazare, M., Scinocca, J. F., Gillett, N. P., et al. (2019). The Canadian Earth System Model Version 5 (CanESM5.0.3). *Geoscientific Model Development*, *12*(11), 4823–4873. https://doi.org/10.5194/gmd-12-4823-2019

Taylor, K. E., Stouffer, R. J., & Meehl, G. A. (2012). An overview of CMIP5 and experiment design. *Bulletin of the American Meteorological Society*, *93*(4), 485–498. https://doi.org/10.1175/BAMS-D-11-00094.1

Trenberth, K. E. (2011). Changes in precipitation with climate change. *Climate Research*, *47*, 123–138. https://doi.org/10.3354/cr00953

Trenberth, K. E., Dai, A., Rasmussen, R. M., & Parsons, D. B. (2003). The changing character of precipitation. *Bulletin of the American Meteorological Society*, *84*(9), 1205–1218. https://doi.org/10.1175/BAMS-84-9-1205

van Haren, R., Haarsma, R. J., de Vries, H., van Oldenborgh, G. J., & Hazeleger, W. (2015). Resolution dependence of circulation forced future central European summer drying. *Environmentral Research Letters*, *10*, 055002. https://doi.org/10.1088/1748-9326/10/5/055002

van Haren, R., Haarsma, R. J., van Oldenborgh, G. J., & Hazeleger, W. (2015). Resolution dependence of European precipitation in a state-of-the-art atmospheric general circulation model. *Journal of Climate*, *28*(13), 5134–5149. https://doi.org/10.1175/JCLI-D-14-00279.1

Voldoire, A., Saint-Martin, D., Sénési, S., Decharme, B., Alias, A., Chevallier, M., et al. (2019). Evaluation of CMIP6 DECK experiments with CNRM-CM6-1. *Journal of Advances in Modeling Earth Systems*, *11*(7), 2177–2213. https://doi.org/10.1029/2019MS001683

Westra, S., Alexander, L. V., & Zwiers, F. W. (2013). Global increasing trends in annual maximum daily precipitation. *Journal of Climate*, *26*(11), 3904–3918. https://doi.org/10.1175/JCLI-D-12-00502.1

Wu, P., Christidis, N., & Stott, P. (2013). Anthropogenic impact on Earth's hydrological cycle. *Nature Climate Change*, *3*(9), 807–810. https://doi.org/10.1038/nclimate1932

Zelinka, M. D., Myers, T. A., McCoy, D. T., Po-Chedley, S., Caldwell, P. M., Ceppi, P., et al. (2020). Causes of higher climate sensitivity in CMIP6 models. *Geophysical Research Letters*, *47*, e2019GL085782. https://doi.org/10.1029/2019GL085782

Zhang, X., Wan, H., Zwiers, F. W., Hegerl, G. C., & Min, S.-K. (2013). Attributing intensification of precipitation extremes to human influence. *Geophysical Research Letters*, *40*, 5252–5257. https://doi.org/10.1002/grl.51010

References From the Supporting Information

Bechtold, P., Chaboureau, J.-P., Beljaars, A., Betts, A. K., Köhler, M., Miller, M., & Redelsperger, J.-L. (2004). The simulation of the diurnal cycle of convective precipitation over land in a global model. *Quarterly Journal of the Royal Meteorological Society*, *130*(604), 3119–3137. https://doi.org/10.1256/qj.03.103

Betts, A. K. (1986). A new convective adjustment scheme. Part I: Observational and theoretical basis. *Quarterly Journal of the Royal Meteorological Society*, *112*(473), 677–691. https://doi.org/10.1002/qj.49711247307

Bretherton, C. S., McCaa, J. R., & Grenier, H. (2004). A new parameterization for shallow cumulus convection and its application to marine subtropical cloud-topped boundary layers. Part I: Description and 1D results. *Monthly Weather Review*, *132*(4), 864–882. https://doi.org/10.1175/1520-0493(2004)132<0864:ANPFSC>2.0.CO;2

Chikira, M., & Sugiyama, M. (2010). A cumulus parameterization with state-dependent entrainment rate. Part I: Description and sensitivity to temperature and humidity profiles. *Journal of the Atmospheric Sciences*, *67*(7), 2171–2193. https://doi.org/10.1175/2010JAS3316.1

Danabasoglu, G., Lamarque, J.-F., Bacmeister, J., Bailey, D. A., DuVivier, A. K., Edwards, J., et al. (2020). The Community Earth System Model Version 2 (CESM2). *Journal of Advances in Modeling Earth Systems*, *12*, e2019MS001916. https://doi.org/10.1029/2019MS001916

Emanuel, K. A. (1991). A scheme for representing cumulus convection in large-scale models. *Journal of the Atmospheric Sciences*, *48*(21), 2313–2329. https://doi.org/10.1175/1520-0469%281991%29048%3C2313%3AASFRCC%3E2.0.CO%3B2

Fritsch, J. M., & Chappell, C. F. (1980). Numerical prediction of convectively driven mesoscale pressure systems. Part I: Convective parameterization. *Journal of the Atmospheric Sciences*, *37*(8), 1722–1733. https://doi.org/10.1175/1520-0469(1980)037<1722:NPOCDM>2.0.CO;2

Gregory, D., & Rowntree, P. R. (1990). A mass flux convection scheme with representation of cloud ensemble characteristics and stability-dependent closure. *Monthly Weather Review*, *118*(7), 1483–1506. https://doi.org/10.1175/1520-0493(1990)118<1483:AMFCSW>2.0.CO;2

Guérémy, J. F. (2011). A continuous buoyancy based convection scheme: One- and three-dimensional validation. *Tellus A: Dynamic Meteorology and Oceanography*, *63*(4), 687–706. https://doi.org/10.1111/j.1600-0870.2011.00521.x

Hack, J. J. (1994). Parameterization of moist convection in the National Center for Atmospheric Research Community Climate Model (CCM2). *Journal of Geophysical Research*, *99*(D3), 5551–5568. https://doi.org/10.1029/93JD03478

Hajima, T., Watanabe, M., Yamamoto, A., Tatebe, H., Noguchi, M. A., Abe, M., et al. (2019). Description of the MIROC-ES2L Earth system model and evaluation of its climate-biogeochemical processes and feedbacks. *Geoscientific Model Development Discussion*, *13*, 2197–2244. https://doi.org/10.5194/gmd-2019-275

Held, I. M., Guo, H., Adcroft, A., Dunne, J. P., Horowitz, L. W., Krasting, J., et al. (2019). Structure and performance of GFDL's CM4.0 climate model. *Journal of Advances in Modeling Earth Systems*, *11*(11), 3691–3727. https://doi.org/10.1029/2019MS001829

Kuhlbrodt, T., Jones, C. G., Sellar, A., Storkey, D., Blockley, E., Stringer, M., et al. (2018). The low-resolution version of HadGEM3 GC3.1: Development and evaluation for global climate. *Journal of Advances in Modeling Earth Systems*, *10*(11), 2865–2888. https://doi.org/10.1029/2018MS001370

Lavery, B., Kariko, A., & Nicholls, N. (1992). A historical rainfall data set for Australia. *Australian Meteorological Magazine*, *40*(1), 33–39.

Mauritsen, T., Bader, J., Becker, T., Behrens, J., Bittner, M., Brokopf, R., et al. (2019). Developments in the MPI-M Earth System Model Version 1.2 (MPI-ESM 1.2) and its response to increasing CO_2. *Journal of Advances in Modeling Earth Systems*, *11*(4), 998–1038. https://doi.org/10.1029/2018MS001400

Mauritsen, T., Stevens, B., Roeckner, E., Crueger, T., Esch, M., Giorgetta, M., et al. (2012). Tuning the climate of a global model. *Journal of Advances in Modeling Earth Systems*, *4*, M00A01. https://doi.org/10.1029/2012MS000154

Mekis, É., & Vincent, L. A. (2011). An overview of the second generation adjusted daily precipitation dataset for trend analysis in Canada. *Atmosphere-Ocean*, *49*(2), 163–177. https://doi.org/10.1080/07055900.2011.583910

Menne, M. J., Durre, I., Vose, R. S., Gleason, B. E., & Houston, T. G. (2012). An overview of the Global Historical Climatology Network-Daily database. *Journal of Atmospheric and Oceanic Technology*, *29*(7), 897–910. https://doi.org/10.1175/JTECH-D-11-00103.1

Nordeng, T. E. (1994). *Extended versions of the convective parameterization scheme at ECMWF and their impact on the mean and transient activity of the model in the tropics*, *ECMWF Technical Memoranda*, (Vol. 206). Shinfield Park, Reading: ECMWF. https://doi.org/10.21957/e34xwhysw

19448007, 2020, 12, Downloaded from https://agupubs.onlinelibrary.wiley.com/doi/10.1029/2019GL086875 by University Of Victoria, Wiley Online Library on [10/04/2025]. See the Terms and Conditions (https://onlinelibrary.wiley.com/terms-and-conditions) on Wiley Online Library for rules of use; OA articles are governed by the applicable Creative Commons License

Park, S., & Bretherton, C. S. (2009). The University of Washington shallow convection and moist turbulence schemes and their impact on climate simulations with the Community Atmosphere Model. *Journal of Climate*, *22*(12), 3449–3469. https://doi.org/10.1175/2008JCLI2557.1

Piriou, J.-M., Redelsperger, J.-L., Geleyn, J.-F., Lafore, J.-P., & Guichard, F. (2007). An approach for convective parameterization with memory: Separating microphysics and transport in grid-scale equations. *Journal of the Atmospheric Sciences*, *64*(11), 4127–4139. https://doi.org/10.1175/2007JAS2144.1

Raymond, D. J., & Blyth, A. M. (1986). A stochastic mixing model for nonprecipitating cumulus clouds. *Journal of the Atmospheric Sciences*, *43*(22), 2708–2718. https://doi.org/10.1175/1520-0469(1986)043<2708:ASMMFN>2.0.CO;2

Raymond, D. J., & Blyth, A. M. (1992). Extension of the stochastic mixing model to cumulonimbus clouds. *Journal of the Atmospheric Sciences*, *49*(21), 1968–1983. https://doi.org/10.1175/1520-0469(1992)049<1968:EOTSMM>2.0.CO;2

Richter, J. H., & Rasch, P. J. (2008). Effects of convective momentum transport on the atmospheric circulation in the Community Atmosphere Model, Version 3. *Journal of Climate*, *21*(7), 1487–1499. https://doi.org/10.1175/2007JCLI1789.1

Seland, Ø., Bensten, M., Graff, L. S., Olivié, D., Toniazzo, T., Gjermundsen, A., et al. (2020). The Norwegian Earth System Model, NorESM2—Evaluation of the CMIP6 DECK and historical simulations. *Geoscientific Model Development Discussion*. https://doi.org/10.5194/gmd-2019-378

Tatebe, H., Ogura, T., Nitta, T., Komuro, Y., Ogochi, K., Takemura, T., et al. (2019). Description and basic evaluation of simulated mean state, internal variability, and climate sensitivity in MIROC6. *Geoscientific Model Development*, *12*(7), 2727–2765. https://doi.org/10.5194/gmd-12-2727-2019

Tiedtke, M. (1989). A comprehensive mass flux scheme for cumulus parameterization in large-scale models. *Monthly Weather Review*, *117*(8), 1779–1800. https://doi.org/10.1175/1520-0493(1989)117<1779:ACMFSF>2.0.CO;2

Volodin, E. M., Mortikov, E. V., Kostrykin, S. V., Galin, V. Y., Lykossov, V. N., Gritsun, A. S., et al. (2017). Simulations of the present-day climate with the climate model INMCM5. *Climate Dynamics*, *49*(11–12), 3715–3734. https://doi.org/10.1007/s00382-017-3539-7

Volodin, E. M., Mortikov, E. V., Kostrykin, S. V., Galin, V. Y., Lykossov, V. N., Gritsun, A. S., et al. (2018). Simulations of the modern climate using the INM-CM48 climate model. *Russian Journal of Numerical Analysis and Mathematical Modeling*, *33*(6), 367–374. https://doi.org/10.1515/rnam-2018-0032

Weller, E., Min, S.-K., Cai, W., Zwiers, F. W., Kim, Y.-H., & Lee, D. (2016). Human-caused Indo-Pacific warm pool expansion. *Science Advances*, *2*, e1501719. https://doi.org/10.1126/sciadv.1501719

Wu, T. (2012). A mass-flux cumulus parameterization scheme for large-scale models: Description and test with observations. *Climate Dynamics*, *38*(3–4), 725–744. https://doi.org/10.1007/s00382-011-0995-3

Wu, T., Lu, Y., Fang, Y., Xin, X., Li, L., Li, W., et al. (2019). The Beijing Climate Center Climate System Model (BCC-CSM): The main progress from CMIP5 to CMIP6. *Geoscientific Model Development*, *12*(4), 1573–1600. https://doi.org/10.5194/gmd-12-1573-2019

Yoshimura, H., Mizuta, R., & Murakami, H. (2015). A spectral cumulus parameterization scheme interpolating between two convective updrafts with semi-Lagrangian calculation of transport by compensatory subsidence. *Monthly Weather Review*, *143*(2), 597–621. https://doi.org/10.1175/MWR-D-14-00068.1

Yukimoto, S., Kawai, H., Koshiro, T., Oshima, N., Yoshida, K., Urakawa, S., et al. (2019). The Meteorological Research Institute Earth System Model Version 2.0, MRI-ESM 2.0: Description and basic evaluation of the physical component. *Journal of the Meteorological Society of Japan Series II*, *97*(5), 931–965. https://doi.org/10.2151/jmsj.2019-051

Zhang, G. J., & McFarlane, N. A. (1995). Sensitivity of climate simulations to the parameterization of cumulus convection in the Canadian climate centre general circulation model. *Atmosphere-Ocean*, *33*(3), 407–446. https://doi.org/10.1080/07055900.1995.9649539

19448007, 2020, 12, Downloaded from https://agupubs.onlinelibrary.wiley.com/doi/10.1029/2019GL086875 by University Of Victoria, Wiley Online Library on [10/04/2025]. See the Terms and Conditions (https://onlinelibrary.wiley.com/terms-and-conditions) on Wiley Online Library for rules of use; OA articles are governed by the applicable Creative Commons License